



Universiteit
Leiden
The Netherlands

Exploring the edge

Contigiani, O.

Citation

Contigiani, O. (2022, January 26). *Exploring the edge*. Retrieved from <https://hdl.handle.net/1887/3254432>

Version: Publisher's Version

License: [Licence agreement concerning inclusion of doctoral thesis in the Institutional Repository of the University of Leiden](#)

Downloaded from: <https://hdl.handle.net/1887/3254432>

Note: To cite this publication please use the final published version (if applicable).

Chapter 5

Dynamical cluster masses from photometric surveys

Traditionally, the masses of galaxy clusters are measured using wide photometric surveys in one of two ways: directly from the amplitude of the weak lensing signal or, indirectly, through the use of scaling relations calibrated using binned lensing measurements. Here, we build on a recently proposed idea and implement an alternative method based on the radial profile of the satellite distribution. This technique relies on splashback, a feature associated with the apocenter of recently accreted galaxies that offers a clear window into the phase-space structure of clusters without the use of velocity information. We carry out this measurement in the stacked satellite distribution around a sample of luminous red galaxies in the fourth data release of the Kilo-Degree Survey and validate our results using abundance-matching masses. To illustrate the power of this measurement, we combine this dynamical mass measurement with lensing mass estimates to robustly constrain scalar-tensor theories of gravity at cluster scales. Our results exclude departures from General Relativity of order unity. Finally, we conclude by rescaling our results and discussing how stage-IV photometric surveys will use splashback to provide percentage level cluster masses at high redshifts.

5.1 Introduction

Today the majority of ordinary matter, a.k.a. baryonic matter, is trapped inside the potential wells of the large-scale structure of the Universe. The main constituent of this invisible scaffolding is dark matter, and most of the mass in the Universe is concentrated in its fully collapsed overdensities, known as halos. At first order, the relationship between dark matter structures and galaxies is simple, and the result of their joint evolution is a tight relationship between the luminosity of a galaxy and the mass of the dark matter halo it inhabits. Because halos are perturbations on top of a background of constant density, their size is usually quantified in terms of overdensity masses. For example, $M_{200\text{m}}$ is defined as the mass contained within a sphere of radius $r_{200\text{m}}$ such that the average density within it is 200 times the average matter density of the Universe $\rho_{\text{m}}(z)$,

$$M_{200\text{m}} = 200 \times \frac{4\pi}{3} \rho_{\text{m}}(z) r_{200\text{m}}^3. \quad (5.1)$$

Dark matter structures are not isolated, however, and the process of structure formation is known to be hierarchical (Press and Schechter, 1974). This means that smaller halos collapsed first and became subhalos once they were accreted onto larger structures. Unsurprisingly, baryonic matter also followed this process, which resulted in today's clusters of galaxies. These represent the largest halos in the Universe and they are still accreting matter from the surrounding environment, i.e. they are not fully virialized yet.

Observationally, the distribution of galaxies in the sky is divided into two populations: red and blue (Strateva et al., 2001). Red galaxies derive their color from their aging stellar population, whereas blue galaxies display active star formation, and young stars dominate their light. The exact mechanism behind quenching, i.e. the transition from star-forming to “red and dead”, is still not fully understood (see e.g. Schaye et al., 2010; Trayford et al., 2015), but it is known to be connected to both baryonic feedback (see e.g. Somerville et al., 2008; Schaye et al., 2010) and interactions inside the dense cluster environment (see e.g. Larson et al., 1980; Moore et al., 1996; van den Bosch et al., 2008). An important consequence of this environmental dependence is the formation of a red sequence, i.e. a close relationship between the color and magnitude of red galaxies in clusters. By calibrating this red sequence as a function of redshift, it is possible to identify clusters in photometric surveys, even in the absence of precise spectroscopic redshifts (Gladders and Yee, 2000).

In recent years, splashback has been recognized as a feature located at the edge of galaxy clusters. The radius of this boundary, r_{sp} , is close to the apocenter of recently accreted material (see e.g. Adhikari et al., 2014; Diemer, 2017; Diemer et al., 2017) and it is associated with a sudden drop in density. This is because it naturally separates the single and multi-stream regions of galaxy clusters: orbiting material piles up inside this radius, while collapsing material located outside it is entering the cluster for

the first time. In simulations and observations, the distribution of red satellite galaxies and dark matter seem to trace this feature in the same fashion (Contigiani et al., 2021; O’Neil et al., 2021), but a possible dependence on satellite properties is still mostly unexplored (Shin et al., 2021). Nonetheless, the existence and detectability of this physical feature have theoretical and observational implications for the study of the large-scale structure of the Universe.

From a theory perspective, the splashback radius defines an accurate cluster mass and sidesteps the issue of pseudo evolution due to an evolving $\rho_m(z)$ as a function of redshift z (Diemer et al., 2013; More et al., 2015). Thanks to this property, this definition can be used to create a universal mass function that is valid for a variety of cosmologies (Diemer, 2020a). Moreover, the shape of the matter profile around this feature can also be used to learn about structure formation, the nature of dark matter (Banerjee et al., 2020) and dark energy (Contigiani et al., 2019).

Observationally, one of the most noteworthy applications of splashback is the study of quenching through the measurement of the spatial distribution of galaxy populations with different colors (Adhikari et al., 2020). While notable, this was not the first result, and many other measurements preceded it. Published works can be divided into three groups: those based on targeted weak lensing observations of X-ray selected clusters (Umetsu and Diemer, 2017; Contigiani et al., 2019), those based on the lensing signal and satellite distributions around SZ-selected clusters (see e.g. Shin et al., 2019), and those based on samples constructed with the help of cluster-finding algorithms applied to photometric surveys (see e.g. More et al., 2016; Collaboration, 2018). However, we note that in the case of the last group, the results are difficult to interpret because the splashback signal correlates with the parameters of the cluster detection method (Busch and White, 2017).

In this work, we implement an application of this feature based on Contigiani et al. (2021). The location of the splashback radius is connected to halo mass, and its measurement from the distribution of cluster members can therefore lead to a mass estimate. Because this distribution can be measured without spectroscopy, this means that we can extract a dynamical mass purely from photometric data. In this chapter, we apply this technique to a present-day photometric survey (see Section 5.2), but we also discuss future prospects. To avoid issues related to cluster-finding algorithms, we studied the average distribution of faint galaxies around luminous red galaxies (LRGs) instead of the targets identified through overdensities of red galaxies. If we consider only passive evolution, the observed magnitude of the LRGs can be corrected to construct a sample with constant comoving density (Rozo et al., 2016; Vakili et al., 2019), and, by selecting the brightest among them, we expect to choose the central galaxies of groups and clusters.

We present our analysis in Section 5.3 and produce two estimates of the masses of the halos hosting the LRGs in Section 5.4. The first is based on the splashback feature measured in the distribution of faint galaxies, while the second is based on weak

lensing measurements. After validating these results with two alternative methods in Section 5.5, we conclude our analysis by discussing our measurements in the context of modified models of gravity. We limit ourselves to redshifts $z < 0.55$ here, but the sample constructed in this manner also has implications for the higher redshift range probed by future stage-IV photometric surveys (Albrecht et al., 2006) such as *Euclid* (Laureijs et al., 2011) and the Legacy Survey of Space and Time (LSST, LSST Science Collaboration et al., 2009). This is because at $z \sim 1$, central galaxies are still assembling, and therefore, their identification can be uncertain. Section 5.5.2 discusses these complications in more detail and explores how this method can be used to complement the use of lensing to extract the masses of X-ray (Contigiani et al., 2019) or SZ selected clusters (Shin et al., 2019).

Unless stated otherwise, we assume a cosmology based on the 2015 Planck data release (Collaboration, 2016). For cosmological calculations, we use the Python packages *ASTROPY* (Price-Whelan et al., 2018) and *COLOSSUS* (Diemer, 2018). The symbols R and r_{sp} always refer to a comoving projected distance and a comoving splashback radius.

5.2 Data

This section introduces both the Kilo-Degree Survey (KiDS, de Jong et al., 2013) and its infrared companion, the VISTA Kilo-degree INfrared Galaxy survey (VIKING, Edge et al., 2013). Their combined photometric catalog and the sample of LRGs extracted from it (Vakili et al., 2020) are the essential building blocks of this chapter.

5.2.1 KiDS

KiDs is a multi-band imaging survey in four filters (*ugri*) covering 1350 deg^2 . Its fourth data release (DR4, Kuijken et al., 2019) is the basis of this chapter and has a footprint of 1006 deg^2 split between two regions located in the north and south Galactic caps (770 deg^2 after masking). The 5σ mean limiting magnitudes in the *ugri* bands are, respectively, 24.23, 25.12, 25.02, and 23.68. The mean seeing for the *r*-band data used both as a detection band and for the weak lensing measurements is $0.7''$. VIKING covers the same footprint in five infrared bands, *ZYJHK_s*.

The raw data have been reduced with two separate pipelines, THELI (Erben et al., 2005) for a lensing-optimized reduction of the *r*-band data, and AstroWISE (McFarland et al., 2013), used to create photometric catalogs of extinction corrected magnitudes. The source catalog for weak lensing analyses was produced from the THELI images and lensfit (Miller et al., 2013; Fenech Conti et al., 2017; Kannawadi et al., 2019) was used to extract the galaxy shapes.

5.2.2 LRGs

The LRG sample presented in Vakili et al. (2020) is based on KiDS DR4. There, the red sequence up to redshift $z = 0.8$ was obtained by combining spectroscopic data with the *griZ* photometric information provided by the two surveys mentioned above. Furthermore, using the near-infrared K_s band from VIKING allowed for a clean separation of stellar objects and considerably lowered the stellar contamination of the sample.

The color-magnitude relation that applies to red galaxies allows the redshifts of LRGs to be calibrated to a precision higher than generic photometric redshifts (photo-*zs*) resulting in redshift errors for each galaxy below $\sigma_z \lesssim 0.02$. For more details on how the total LRG sample is defined and its broad properties, we direct the interested reader to Vakili et al. (2020), or Vakili et al. (2019), a similar work based on a previous KiDS data release.

Fortuna et al. (2021) further analyzed this same catalog and calculated absolute magnitudes for all LRGs using LEPHARE (Arnouts and Ilbert, 2011) and EZGAL (Mancone and Gonzalez, 2012). The first code corrects for the redshift of the rest-frame spectrum in the different passbands (k-correction), while the second corrects for the passive evolution of the stellar population (e-correction). For this work, we used these (k+e)-corrected luminosities as a tracer of total mass since the two are known to be highly correlated (see e.g. Mandelbaum et al., 2006; van Uitert et al., 2015). Based on this, we then defined two samples with different absolute r-band magnitude cuts, $M_r < -22.8$ and $M_r < -23$, that we refer to as *all* and *high-mass* samples. These are the 10 and 5 percentile of the absolute magnitude distribution of the *luminous* sample studied in Fortuna et al. (2021), and the two samples contain 5524 and 2850 objects each.

Because the (k+e)-correction presented above is designed to create a redshift independent sample, the expected redshift distribution of the LRGs should correspond to a constant comoving density. However, when studying our samples (see Figure 5.1), it is clear that this assumption holds only until $z = 0.55$. This suggests that the empirical corrections applied to the observed magnitudes are not optimal. We stress that this discrepancy was not recognized before because our selection amplifies it: we considered the tail of a much larger sample ($N \sim 10^5$) with a steep magnitude distribution, for which a small error in the lower limit induced a large mismatch at the high-luminosity end. We discard all LRGs above $z = 0.55$ and after fitting the distributions in Figure 5.1, we obtained comoving densities $n = 7.5 \times 10^{-6} \text{ Mpc}^{-3}$ and $n = 4.0 \times 10^{-6} \text{ Mpc}^{-3}$ for the full and the high-mass samples respectively.

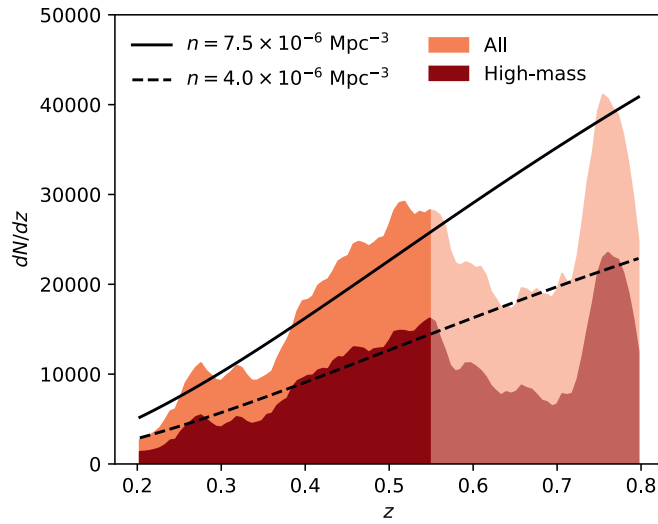


Figure 5.1: The redshift distributions of the LRG samples studied in this chapter. As visible in the figure, the distributions are consistent with the assumption of a constant comoving density up to redshift $z = 0.55$, the maximum considered here. The empirical selection criteria were explicitly designed to select for constant comoving density fail for higher redshifts.

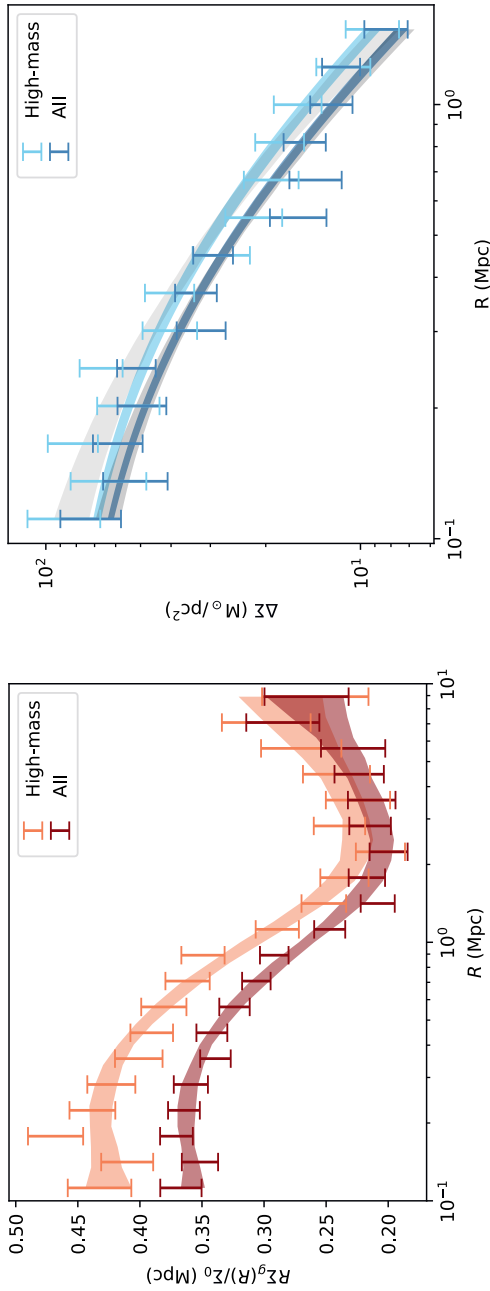


Figure 5.2: The signals studied in this chapter. We measure the number density of faint red galaxies (left panel) and the lensing signal (right panel) around the LRGs in our sample (*all*) and its high-luminosity subsample (*high-mass*). Both measurements are based on the KiDS photometric catalog. The steep drop around 1 Mpc visible in the left panel is the splashback feature, and it is connected to the total mass of the LRG halos. Similarly, the amplitude of the lensing signal on the right is also a measure of the same mass. In addition to the data and the 1σ error bars, we also display the 68 percent contours of a profile fit performed to extract the mass measurements. The fit on the right is performed either by varying only the amplitude of the signal (thinner contours) or by varying its amplitude and concentration (wider contours). See text for more details. Section 5.2 presents the data and the two samples, Section 5.3 discusses how the profiles are measured, and Section 5.4 discusses the fitting procedure.

5.3 Profiles

In this section, we discuss how we used the data introduced in the previous section to produce two stacked signals measured around the LRGs: the galaxy profile, capturing the distribution of faint red galaxies, and the weak lensing profile, a measure of the projected mass distribution extracted from the distorted shapes of background galaxies. We present these two profiles and the 68 percent contours of two separate parametric fits in Figure 5.2. The details of the fitting procedure are explained in Section 5.4.

5.3.1 Galaxy profile

We expect bright LRGs to be surrounded by fainter satellites, i.e. we expect them to be the central galaxies of galaxy groups or clusters. We focused in particular on the distribution of red satellites as this is the most abundant population in galaxy clusters and, due to their repeated orbits, they are known to trace dynamical features such as splashback better (see e.g. Baxter et al., 2017). To obtain the projected number density profile of these surrounding galaxies, we split the LRG samples in 7 redshift bins of size $\delta_z = 0.05$ in the range $z \in [0.2, 0.55]$. We then defined a corresponding KiDS galaxy catalog for each redshift bin, obtained the background-subtracted distribution of these galaxies around the LRGs, and finally stacked these distributions using the weights w_i defined below.

The KiDS catalogs used in this process were based on two redshift-dependent selections: in magnitude and color. The reason behind the first selection is simple: compared to a flat signal-to-noise (SNR) threshold, a redshift-dependent magnitude limit does not mix populations with different intrinsic magnitudes as a function of redshift (as suggested by More et al., 2016). On the other hand, the color cut is more physical since we are only interested in the distribution of red galaxies. Combining a color cut and a magnitude cut means choosing a similar population across redshifts, even in the absence of k-corrected magnitudes for the KiDS galaxies. Finally, we point out that we did not select the photo-zs of the KiDS galaxies as this is unnecessary.

For the highest redshift considered here, z_{\max} , we limited ourselves to observed magnitudes $m_r < 23$, equivalent to a 10σ SNR cut. We then extrapolated this limit to other redshift bins by imposing

$$m_r < 23 - 5 \log \left(\frac{d_L(z_{\max})}{d_L(z_i)} \right), \quad (5.2)$$

where z_i is the upper edge of the redshift bin considered, and $d_L(z)$ is the luminosity distance as a function of redshift. Afterward, we divided the galaxy catalogs into two-color populations by following the method of Adhikari et al. (2020). Compared to random points in the sky, the color distribution of KiDS galaxies around LRGs contains two features: an overdensity of "red" objects and a deficit of "blue" objects. Based on

the red-sequence calibration of Vakili et al. (2020) and the location of the 4000 Å break, we identified the $(g - r) - (r - i)$ plane as the most optimal color space to separate these two population at redshifts $z \leq 0.55$. The two classes can then be separated by the line perpendicular to the segment connecting these two loci and passing through its midpoint. We note that the $(i - Z) - (r - i)$ plane would be better suited for higher redshifts.

We used TREECORR (Jarvis et al., 2004; Jarvis, 2015) to extract the correlation functions from the catalogs defined above

$$\xi_i = \frac{DD_i}{DR_i} - 1, \quad (5.3)$$

where DD and DR are the numbers of LRG-galaxy pairs calculated using the KiDS catalogs or the random catalogs, respectively. These randoms are composed of points uniformly distributed in the KiDS footprint. We then produced covariance matrices by dividing our survey area into 50 equal-areal jackknife regions to provide an error on the binned radial signal. Because the signal is statistics limited, we can ignore the negligible off-diagonal terms of this matrix. To support this statement, we point out that due to the low number density of the sample (see Figure 5.1), the clusters do not overlap in real space.

Formally, the correlation function written above is related to the surface overdensity of galaxies:

$$\Sigma_i(R) = \xi_i(R) \Sigma_{0,i}, \quad (5.4)$$

where $\Sigma_{0,i}$ is the average surface density of KiDS galaxies in the i -th redshift bin. However, since we are interested in the shape of the profile and not its amplitude, we did not take this into account when stacking the correlation functions ξ_i . To optimize the measurement, we use as weights w_i the inverse variance of our measurement. This corresponds to an SNR weighted average, where the SNR is, in our case, dominated by the statistical error of the DD counts. Formally:

$$\frac{\Sigma_g(R)}{\Sigma_0} = \frac{\sum_i w_i \xi_i(R)}{\sum_i w_i}, \quad (5.5)$$

where Σ_0 is a constant needed to transform the dimensionless correlation function into the projected mass density. Because we decided to fit the combination $\Sigma_g(R)/\Sigma_0$ directly, the value of this constant is unimportant.

The left side of Figure 5.2 presents our measurement of the galaxy profile around the LRGs. As expected, the high-mass subsample has a higher amplitude compared to the entire sample.

5.3.2 Weak lensing profile

The shapes of background sources are deformed, i.e. lensed, by the presence of matter along the line of sight. In the weak lensing regime, this results in the observed ellipticity

ϵ of a galaxy being a combination of its intrinsic ellipticity and a lensing shear. If we assume that the intrinsic shapes of galaxies are randomly oriented, we can then measure a coherent shear in a region of the sky by computing the mean of the ellipticity distribution.

Consider a circularly symmetric matter distribution acting as a lens. In this case, the shear is only tangential, i.e. the shapes of background galaxies are deformed only in the direction parallel and perpendicular to the line in the sky connecting the source to the center of the lens. Therefore, we can define the lensing signal in an annulus of radius R as the average value of the tangential components of the ellipticities $\epsilon^{(t)}$. Below, we describe the exact procedure we followed to measure this signal for the LRGs samples using the KiDS source catalog extending up to redshift $z = 1.2$ (see also, Viola et al., 2015; Dvornik et al., 2017).

Based on the *lensfit* weights w_s associated with each source, we defined *lensing* weights for every lens-source combination,

$$w_{l,s} = w_s \left(\Sigma_{\text{crit},l}^{-1} \right)^2, \quad (5.6)$$

where the two indices l and s are used to indicate multiple lens-source pairs if more than one lens is considered. The second factor in the product above represents a lensing efficiency contribution and, in our formalism, this quantity does not depend on the source. It is calculated instead as an average over the entire source redshift distribution $n(z_s)$:

$$\Sigma_{\text{crit},l}^{-1} = \frac{4\pi G}{c^2} \frac{d_A(z_l)}{(1+z_l)^2} \int_{z_l+\delta}^{\infty} dz_s \frac{d_A(z_l, z_s)}{d_A(0, z_s)} n(z_s), \quad (5.7)$$

where $d_A(z_1, z_2)$ is the angular diameter distance between the redshifts z_1 and z_2 in the chosen cosmology. Sources that belong to the correlated structure surrounding the lens might scatter behind it due to the uncertainty of photo-zs. The gap between the lens plane and the source plane in the expression above ($\delta = 0.2$) is there to make sure our signal is not diluted by this effect (see appendix A4 of Dvornik et al., 2017). The additional factor $(1+z_l)$ in this expression is there because we are working in comoving coordinates. Once all of the ingredients are computed, an estimate of the measured lensing signal is given by:

$$\Delta\Sigma(R) = \frac{\sum_{l,s} \epsilon_{l,s}^{(t)} w_{l,s} \Sigma_{\text{crit},l}}{\sum_{l,s} w_{l,s}} \frac{1}{1+m}, \quad (5.8)$$

where the sums are calculated over every source-lens pair, and m is a residual multiplicative bias of order 0.014 calibrated using image simulations (Fenech Conti et al., 2017; Kannawadi et al., 2019). This signal is connected to the mass surface density $\Sigma_m(R)$ and its average value within that radius, $\overline{\Sigma}_m(< R)$.

$$\Delta\Sigma(R) = \overline{\Sigma}_m(< R) - \Sigma_m(R). \quad (5.9)$$

The covariance matrix of this average lensing signal was extracted through bootstrapping, i.e. by resampling 10^5 times the $1006 \, 1 \times 1 \, \text{deg}^2$ KiDS tiles used in the analysis. This signal, like the galaxy profile before, is also statistics limited. Therefore we have not included the negligible off-diagonal terms of the covariance matrix in our analysis.

Finally, we note that we have thoroughly tested the consistency of our lensing measurement. The average cross-component lensing signal is expected to be zero. To confirm that this is true for our results, we computed the expression in Equation (5.8) using the cross-component $\epsilon^{(\times)}$ instead of the tangential $\epsilon^{(t)}$ and verified that its value was consistent with zero. Similarly, we also confirmed that the measurement was not affected by additive bias by measuring the lensing signal evaluated around random points.

5.4 Four ways to measure cluster masses

This section discusses how we have obtained two independent measures of the total mass contained in the LRG halos by fitting parametric profiles to the signals extracted in the previous section. We measured two quantities: a dynamical mass and a lensing mass. The first is connected to the splashback feature seen in the distribution of satellite galaxies, while the second one is connected to the amplitude of the lensing signal (see Figure 5.2).

5.4.1 Splashback mass

By fitting the galaxy distribution with a flexible model, it is possible to estimate the total halo mass. The essential feature that such a three-dimensional profile, $\rho(r)$, must capture is a sudden drop in density around $r_{200\text{m}}$ and its most important parameter is the point of steepest slope, also known as the splashback radius r_{sp} . Equivalently, this can be defined as the radius where the function $d \log \rho / d \log r$ reaches its minimum.

In general, the average projected correlation function can be written in terms of the average three-dimensional mass density profile as:

$$\frac{\Sigma_{\text{g}}(R)}{\Sigma_0} = \frac{2}{\Sigma_0} \int_0^\infty d\Delta \rho \left(\sqrt{\Delta^2 + R^2} \right), \quad (5.10)$$

In practice, we evaluated this integral in the range $[0, 40]$ Mpc, but we have also confirmed that our results are not sensitive to the exact value of the upper integration limit.

The specific density profile that we used is based on Diemer and Kravtsov (2014),

Parameter	Prior
α	$\mathcal{N}(0.2, 2)$
g	$\mathcal{N}(4, 0.2)$
β	$\mathcal{N}(6, 0.2)$
$r_t/(1 \text{ Mpc})$	$\mathcal{N}(1, 4)$
s_e	$[0.1, 2]$

Table 5.1: The priors used in the fitting procedure of Section 5.4. When fitting the data in the left panel of Figure 5.2, we employ the model in Equation (5.11) with the priors presented above. For some parameters, we impose flat priors in a range, e.g. $[a, b]$, while for others we impose a Gaussian prior $\mathcal{N}(m, \sigma)$ with mean m and standard deviation σ . We do not restrict the prior range of the two degenerate parameters $\bar{\rho}$ and r_0 .

and it has the following form:

$$\rho(r) = \rho_{\text{Ein}}(r)f_{\text{trans}}(r) + \rho_{\text{out}}(r), \quad (5.11)$$

$$\rho_{\text{Ein}}(r) = \rho_s \exp \left(-\frac{2}{\alpha} \left[\left(\frac{r}{r_s} \right)^\alpha - 1 \right] \right), \quad (5.12)$$

$$f_{\text{trans}}(r) = \left[1 + \left(\frac{r}{r_t} \right)^\beta \right]^{-g/\beta}, \quad (5.13)$$

$$\rho_{\text{out}} = \bar{\rho} \left(\frac{r}{r_0} \right)^{-s_e}. \quad (5.14)$$

These expressions define a profile with two components: an inner halo and an infalling region. The term $\rho_{\text{Ein}}(r)f_{\text{trans}}(r)$ represents the collapsed halo through a truncated Einasto profile with shape parameter α and amplitude ρ_s (Einasto, 1965). The parameters g, β in the transition function determine the maximum steepness of the sharp drop between the two regions, and r_t determines its approximate location. Finally, the term $\rho_{\text{out}}(r)$ describes a power-law mass distribution with slope s_e and amplitude $\bar{\rho}$, parametrizing the outer region dominated by infalling material. For more information about the role of each parameter and its interpretation, we refer the reader to Diemer and Kravtsov (2014), and previous measurements presented in the introduction (see e.g. Contigiani et al., 2019, for more details about the role of the truncation radius r_t).

To extract the location of the splashback radius for our two LRG samples, we fitted this model profile to the correlation function data using the ensemble sampler EMCEE (Foreman-Mackey et al., 2013). The priors imposed on the various parameters are presented in Table 5.1, and we highlight in particular that the range for α is a generous scatter around the expectation from numerical simulations (Gao et al., 2008).

In clusters, it is possible for the location of the central galaxy to not correspond to

the barycenter of the satellite distribution. This discrepancy is usually accounted for in the modeling of the projected distribution in Equation (5.10), but we chose not to consider this effect in our primary analysis. This is justified because the miscentering term affects the profile within $R \sim 0.1$ Mpc, while we are interested in the measurement around $R \sim 1$ Mpc (Shin et al., 2021), and the data do not require a more flexible model to provide a good fit.

Finally, to transform the r_{sp} measurements into a value for $M_{200\text{m}}$, we used the relations from Diemer (2020b), evaluated at our median redshift of $\bar{z} = 0.44$. Because the splashback radius has a dependence on accretion rate, we used the median value of this quantity as a function of mass as a proxy for the effective accretion rate of our stacked sample. We note in particular that the additional scatter introduced by the accretion rate and redshift distributions is expected to be subdominant given the large number of clusters we have considered. We best fitting profiles and error intervals of the inferred $M_{200\text{m}}$ are shown in Figure 5.2.

5.4.2 Lensing mass

To extract masses from the lensing signal, we performed a fit using an NFW profile (Navarro et al., 1996, 1997):

$$\rho(r) = \frac{1}{4\pi F(c_{200\text{m}})} \frac{M_{200\text{m}}}{r(r + r_{200\text{m}}/c_{200\text{m}})^2}, \quad (5.15)$$

where $M_{200\text{m}}$ and $r_{200\text{m}}$ are related by Equation (5.1), $c_{200\text{m}}$ is the halo concentration, and the function appearing in the first term is defined as:

$$F(c) = \ln(1 + c) - c/(1 + c). \quad (5.16)$$

From this three-dimensional profile, the lensing signal can be derived using Equations (5.9) and (5.10) by replacing Σ_{m} with $\Sigma_{\text{g}}/\Sigma_0$.

Because the mass and concentration of a halo sample are related, several mass-concentration relations calibrated against numerical simulations are available in the literature. We chose to fit an NFW profile because these mass-concentration relations are usually given in terms of its parameters, and imposing such constraint increases the precision of the measurement by forcing a strong prior on the shape of the profile. Notice that we could have used the complex model of Equation (5.11) also for the lensing measurement. However, the differences between the Einasto profile used there and the NFW profile presented above are not expected to induce systematic biases at the precision of our measurements (see e.g. Sereno et al., 2016). Although extra complexity might not be warranted, particular care should still be taken when measuring profiles at large scales, where the difference between the more flexible profile and a traditional NFW profile is more pronounced. Consequently, we reduce the bias in our measurement by fitting only projected distances $R < 1.5$ Mpc, where the upper limit is decided based on the r_{sp} inferred by our galaxy distribution measurement.

For the measurement presented in this section, we use the mass-concentration relation of Bhattacharya et al. (2013). However, because this relation is calibrated with numerical simulations based on a different cosmology, we also fit the lensing signal while keeping the concentration as a free parameter. This consistency check is particularly important because halo profiles are not perfectly self-similar (Diemer and Kravtsov, 2015) and moving between different cosmologies or halo mass definitions might require additional calibration. We perform the fit to the profiles in the right panel of Figure 5.2 using the median redshift of our samples, $\bar{z} = 0.44$. We find that statistical errors dominate the uncertainties, and we do not measure any systematic effect due to the assumed mass-concentration relation.

5.4.3 Supplementary mass measurements

In addition to the two mass measurements extracted from the galaxy and lensing profiles, we discuss the predictions we obtained from two additional methods. The first is based on an abundance matching argument, while the second is based on the clustering properties of our LRG sample. We focus on these two methods to estimate masses because, similarly to the main two methods, they can also be performed in the presence of photometric data alone.

For the abundance-matching mass, we used the mass function of Tinker et al. (2008) at the median redshift $\bar{z} = 0.44$ to convert the comoving densities from Figure 5.1 into lower limits on the halo mass M_{200m} . To complete the process, we then extracted the mean mass of the sample using the same mass function.

For the clustering mass, we used the large-scale distribution of our sample as a proxy. Because the spatial correlation function of halos depends on their mass, we can estimate the average mass of our cluster sample by extracting the bias of this population with respect to the matter distribution of the Universe. To this end, we divided the LRG sample into three equally populated redshift bins and computed the angular autocorrelation functions within a range of scales. For the lower limit, we used $R = 10$ Mpc to make sure we considered only linear scales. For the upper limit, we used $\theta = 150$ arcmin to satisfy the flat-sky approximation and to accurately account for cosmic variance within the limited KiDS footprint. We converted between projected radii and angular distances using our assumed cosmology and measured the autocorrelation function using the same procedure presented in Section 5.3.1. However, we did take into account the off-diagonal terms of the covariance matrix in this case since the uncertainties at large scales are dominated by sample variance.

Using the Limber approximation (Limber, 1953), the measured angular autocorrelation function of the i -th LRG bin can be written as

$$\Theta_i(R|M) = \int dz \frac{n_i^2(z)}{d\chi/dz} b^2(M_{200m}) \int_{-\infty}^{+\infty} d\Delta \xi(\sqrt{R^2 + \Delta^2}, z), \quad (5.17)$$

where $\xi(r, z)$ is the matter correlation function in terms of the comoving distance r and redshift z , $b(M_{200\text{m}})$ is the bias as a function of mass from Tinker et al. (2010), $\chi(z)$ is the comoving distance to redshift z , and $n_i(z)$ is the normalized redshift distribution of the LRGs in the considered bin. This latter distribution was obtained by taking into account the redshift uncertainties of the red-sequence calibration (see Section 5.2.2). The clustering mass was measured by fitting this model to the three LRG bins assuming a constant value of $M_{200\text{m}}$ throughout the entire redshift range.

We note that Vakili et al. (2020) has shown that the distribution of LRGs at the scales considered in this section can be strongly affected by survey systematics, and specific weights should be used when computing the clustering properties. We have verified that the autocorrelation signals of our samples are unaffected by the use of these weights. In general, fainter objects are more impacted by the varying depth introduced by survey systematics since they can scatter in or out of the detection threshold.

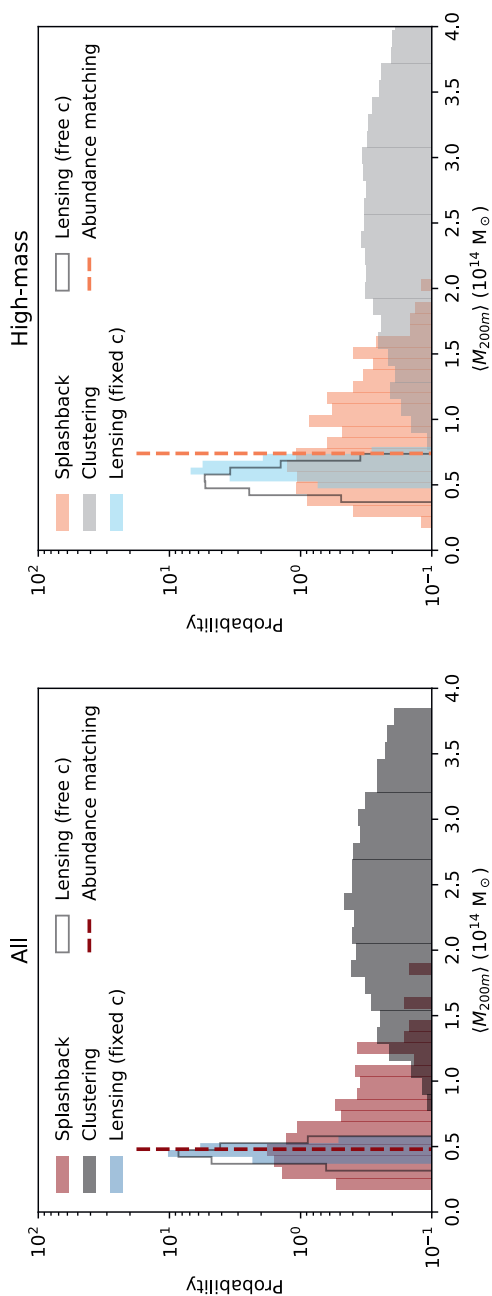


Figure 5.3: Comparison of the mass measurements performed in this chapter. Using four different techniques, we measured the mass of the halos hosting our LRG sample (*all*) and a high-luminosity subsample (*high-mass*). The remarkable consistency between the four methods for both samples is a testament to the robustness of our LRG selection and the power of the splashback feature in providing cluster masses. Table 5.2 reports the same results in textual form. See Section 5.5 for more details about this comparison.

Technique	M_{200m} ($10^{14} M_{\odot}$)		r_{sp} (Mpc)	
	All	High-mass	All	High-mass
Splashback	$0.57^{+0.73}_{-0.22}$	$0.77^{+0.64}_{-0.30}$	1.48 ± 0.28	1.6 ± 0.25
Lensing (fixed c)	0.46 ± 0.03	0.62 ± 0.05	1.40 ± 0.01	1.52 ± 0.02
Lensing (free c)	0.44 ± 0.05	0.54 ± 0.07	1.39 ± 0.03	1.6 ± 0.04
Abundance	0.48	0.74	1.42	1.6
Clustering	2.41 ± 0.94	2.62 ± 1.18	—	—

Table 5.2: The mass measurements performed in this chapter. This table summarizes the discussion of Section 5.5 and the measurements presented in Figure 5.3 for our LRG samples (*all* and *high-mass*). The quoted splashback radii are in comoving coordinates. The abundance-matching measurements are provided without error bars as we have not modeled the selection function of our LRGs. Since the clustering method is not informative, we do not present a splashback radius estimate based on it. Most measurements and conversions between M_{200m} and r_{sp} (see the end of Section 5.4.1 for details) are computed using a model at the median redshift $\bar{z} = 0.44$, identical for both samples. The bias measurements take into account a redshift-dependent clustering but assume a constant halo mass.

5.5 Discussion

In this section, we compare and validate the measurements presented in the previous one, see Figure 5.3 and Table 5.2 for a quick summary of our main conclusions. As an example of the power granted by multiple cluster mass measurements from the same survey, we also present an interpretation of these measurements in the context of modified theories of gravity.

In Figure 5.3 and Table 5.2, we present the results of our two main mass measurements combined with the two extra introduced in the previous subsection. All measurements are in agreement, providing evidence that there is no significant correlation between the selection criteria of our LRG sample and the measurements performed here.

The first striking result is the varying degree of precision among the different measurements. The lensing measurement is the most precise, even when the concentration parameter is allowed to vary. In particular, the fact that the inferred profiles do not exhaust the freedom allowed by error bars in the right-hand panel of Figure 5.2 implies that our model prior is responsible for the strength of our measurement and that a more flexible model will result in larger mass uncertainties. On the other hand, with splashback, we can produce a dynamical mass measurement without any knowledge of the shape of the average profile and, more importantly, without having to capture the exact nature of the measured scatter. In the end, the inferred average splashback mass of our high-mass LRG sample has an uncertainty of around 50 percent. This is significantly

higher than the lensing measurement but still considerably better than the clustering measurement, consistent with zero mass. Our results show that the sparsity of high-density peaks does not allow clustering to provide competitive mass constraints. This is despite the naive expectation that the clustering of massive halos should depend only on their overdensity, or, equivalently, that they are not affected by assembly bias (Sheth and Tormen, 2004).

As a final note on our results, we point out that the difference between the masses of the two samples (*all* and *high-mass*) is 2σ for the lensing measurement, but it is not even marginally significant for the splashback values (due to the large error bars). As already shown in Contigiani et al. (2019), splashback measurements are heavily weighted towards most massive objects. To produce a non-mass weighted measure of the splashback feature, it is necessary to rescale the individual profiles with a proxy of the halo mass. However, because the study of r_{sp} as a function of mass is not the focus of this work, we leave this line of study open for future research.

5.5.1 Gravitational constants

In this section, we present how the combination of the lensing masses and splashback radii measured in the section above can be used to constrain models of gravity. The principle behind this constraint is the fact that, while General Relativity (GR) predicts that the trajectories of light and massive particles are affected by the same metric perturbation, extended models generally predict a discrepancy between the two.

In extended models, the equations for the linearized-metric potentials (Φ and Ψ , see Bardeen, 1980) can be connected to the background-subtracted matter density $\rho(x)$ through the following equations (Amendola et al., 2008; Bertschinger and Zukin, 2008; Pogosian et al., 2010),

$$\nabla^2(\Phi + \Psi) = 8\pi G\Sigma(x)\rho(x), \quad (5.18)$$

$$\nabla^2\Phi = 4\pi G\mu(x)\rho(x). \quad (5.19)$$

In the expressions above, the functions μ and Σ , also known as G_{matter}/G and G_{light}/G can be in principle a function of space and time (collectively indicated by x). We stress that the symbol Σ , previously used to refer to projected three-dimensional distributions (Σ_g, Σ_m), has a different use in this context. These equations are expressed in terms of Φ and $\Phi + \Psi$ because the trajectories of particles are affected by the first, while the deflection of light is governed by the second. In the presence of only non-relativistic matter, Einstein's equations in GR reduce to $\Phi = \Psi$ and we have $\Sigma = \mu = 1$.

The same type of deviation from GR can also be captured in the post-Newtonian parametrization by a multiplicative factor γ between the two potentials: $\Psi = \gamma\Phi$. If μ , Σ , and γ are all constants, the three are trivially related:

$$\frac{\mu}{\Sigma} = \frac{1 + \gamma}{2}. \quad (5.20)$$

Under this same assumption, the ratio between the masses measured through lensing and the mass measured through the dynamics of test particles (e.g. faint galaxies or stars) can be used to constrain these parameters and the literature contains multiple results concerning these extended models. Solar System experiments have constrained γ to be consistent with its GR value ($\gamma = 1$) up to 5 significant digits (Bertotti et al., 2003), but the current measurements at larger scales are substantially less precise. For kpc-sized objects (galaxy-scale), stellar kinematics have been combined with solid lensing measurements to obtain 10 percent constraints (Bolton et al., 2006; Collett et al., 2018), while large-scale measurements ($\sim 10 - 100$ Mpc) can be obtained by combining cosmic shear and redshift space distortion measurements to achieve a similar precision (see e.g. Simpson et al., 2013; Joudaki et al., 2018). As for the scales considered in this chapter, a precision of about 30 percent can be obtained by combining lensing masses with either the kinematics of galaxies inside fully collapsed cluster halos (Pizzuti et al., 2016) or the distribution of hot X-ray emitting gas (Wilcox et al., 2015). However, in this case, the effects of the required assumptions (e.g. spherical symmetry and hydrostatic equilibrium for the gas) are harder to capture. In all cases, no deviation from GR has been measured.

As an example of the power of the measurements presented in Section 5.4, we present here their implication for beyond-GR effects. On one hand, our lensing signal is a measurement of the amplitude $M_{200m, L}$ of the lensing matter density $\rho_L = \rho\Sigma$. On the other hand, the splashback radius r_{sp} depends on the amplitude of $\rho_L \times \mu/\Sigma$ and it is related to the splashback mass $M_{200m, sp}$. We, therefore, focus on the ratio of these two amplitudes measured in the high-mass sample:

$$\frac{\mu}{\Sigma} = \frac{M_{200m, L}}{M_{200m, sp}} = 0.8 \pm 0.4 \quad \Leftrightarrow \quad \gamma = 0.6 \pm 0.8. \quad (5.21)$$

In high-density regions such as the Solar System, the expectation $\gamma = 1$ must be recovered with high precision. Hence, alternative theories of gravity commonly predict scale- and density-dependent effects, which cannot be captured through constant values of μ and Σ . Because r_{sp} marks a sharp density transition around massive objects, it is more suited to test these complicated dependencies. To provide an example of the constraints possible under this second interpretation, we followed Contigiani et al. (2019) to convert the effects of an additional scale-dependent force (also known as a fifth force) on the location of the splashback radius r_{sp} .

In the case of the symmetron gravity theory studied there (Hinterbichler et al., 2011), the change in r_{sp} introduced by the fifth force was obtained by integrating the trajectories of test particles in the presence or absence of this force. In total, the theory has three parameters: 1) the dimensionless vacuum Compton wavelength of the field $\lambda_0/R(t_0)$, that we fix to be 0.05 times the size of the collapsed object; 2) z_{SSB} , the redshift corresponding to the moment at which the fifth force is turned on in cosmic history, that we fix at $z_{SSB} = 1.25$; and 3) f , a dimensionless force-strength parameter

that is zero in GR. The choices of the fixed values that we imposed are based on physical considerations due to the connection of these gravity models to dark energy while maximizing the impact on splashback. See Contigiani et al. (2019) for more details.

To match the expectation of the model to observations, we first converted the $M_{200\text{m}}$ lensing measurement into an expected splashback radius $r_{\text{sp,L}}$ by reversing the procedure explained at the end of Section 5.4.1 and then compared the measured r_{sp} to this value. From the high-mass data, we obtained the following 1σ constraints:

$$\frac{r_{\text{sp,L}} - r_{\text{sp}}}{r_{\text{sp,L}}} = 0.07 \pm 0.20 \quad \implies \quad f < 1.8. \quad (5.22)$$

The symmetron theories associated to $z_{\text{SSB}} \sim 1$ and cluster-sized objects correspond to a coupling mass scale of the order of 10^{-6} Planck masses, a region of the parameter space which is still allowed by the solar-system constraints (Hinterbichler et al., 2011) and which has not been explored by other tests (see e.g. O’Hare and Burrage, 2018; Burrage and Sakstein, 2018). In particular, the upper limit on f produced here directly translates into a constraint on the symmetron field potential of Contigiani et al. (2019).¹ Thus, our result shows that we can test the existence of scalar fields with quite weak couplings and directly project these measurements into a broader theory parameter space.

5.5.2 Future prospects

Our results show that the precision of the recovered splashback mass is not comparable to the low uncertainty of the lensing measurements. Because of this, every constraint based on comparing the two is currently limited by the uncertainty of the first. While this chapter’s focus is not to provide accurate forecasts, we attempt to quantify how we expect these results to improve with larger samples. In particular, we focus our attention on wide stage-IV surveys such as *Euclid* (Laureijs et al., 2011) and LSST (LSST, LSST Science Collaboration et al., 2009).

First, we investigate how our results can be rescaled. In the process of inferring $M_{200\text{m}}$ from r_{sp} , we find that the relative precision of the first is always a multiple (3 – 4) of the second. This statement, which we have verified over a wide range of redshifts ($z \in [0, 1.5]$) and masses ($M_{200\text{m}} \in [10^{13}, 10^{15}] \text{ M}_{\odot}$), is a simple consequence of the low slope of the $M_{200\text{m}} - r_{\text{sp}}$ relation. Second, we estimate the size of a cluster sample we can obtain and how that translates into an improved errorbar for r_{sp} . LSST is expected to reach 2.5 magnitudes deeper than KiDS and to cover an area of the sky 18 times larger (LSST Science Collaboration et al., 2009). Part of this region is covered by the galactic plane and will need to be masked, but the resulting LRG sample will reach up to $z \sim 1.2$ and cover a comoving volume about a factor 100 larger than what

¹However, we stress here that this constraint does not have implications for dark energy, as the model considered there is not able to drive cosmic acceleration in the absence of a cosmological constant.

is considered in this work. Because the selected LRGs are designed to have a constant comoving density, we can use this estimate to scale the error bars of our galaxy profile measurement. A sample $N = 100$ times the size would result in a relative precision in r_{sp} of about 1 percent, which translates into a measured $M_{200\text{m}}$ with a few percentage point uncertainty. This result is obtained by simply rescaling the error bars by a factor $\sqrt{N} = 10$, but notice that the effects do not rescale linearly for r_{sp} . This is still larger than what is allowed by lensing measurements but can easily apply to high-redshift clusters, for which fewer background sources are available.

We note that this simple rescaling sidesteps multiple issues. Here we consider three of them and discuss their implications and possible solutions. 1) At high redshift, color-identification requires additional bands, as the 4000 Å break moves out of the LSST *grizy* filters. 2) Even if we assume that an LRG sample can be constructed, the population of orbiting satellites at high redshift might not necessarily be easy to identify as the read sequence is only beginning to form. 3) Finally, with more depth, we also expect fainter satellites to contribute to the galaxy profile signal, but the details of this population for large cluster samples at high-redshifts are not known. For example, a simple extrapolation of the observed satellite magnitude distribution implies that the number of satellites forming the galaxy distribution signal might be enhanced by a factor 10, but this does not consider, for example, the disruption of faint satellites.

In addition to the forecast for the galaxy profiles discussed above, we also expect a measurement of r_{sp} with a few percentage point uncertainty directly from the lensing profile (Xhakaj et al., 2020). This precision will only be available for relatively low redshifts ($z \sim 0.45$), allowing a precise comparison of the dark matter and galaxy profiles. This cross-check can also be used to understand the effects of galaxy evolution in shaping the galaxy phase-space structure (Shin et al., 2021) and help disentangle the effects of dynamical friction, feedback, and modified models of dark matter (Adhikari et al., 2016; Banerjee et al., 2020).

5.6 Conclusions

In this chapter, we have used the splashback feature to measure the average dynamical mass of halos hosting bright KiDS LRGs. We obtain a precision of 15 percent. To support our result, we have also validated this mass measurement using a simple abundance-matching argument and weak lensing masses (see Figure 5.3 and Table 5.2). We also presented a fourth validation technique based on the linear clustering of halos, but in this case, the low statistics of high-density peaks hindered the constraining power. Finally, as an application of the synergy between the strong lensing and splashback masses, we have provided constraints on models of modified gravity (see Equation 5.22).

The main achievement that we want to stress here is that these self-consistent measurements are exclusively based on and validated with photometric data. The bright

LRG samples employed here can be easily matched to simulations, offer a straightforward interpretation, and, in general, are found to be robust against systematic effects in the redshift calibration (Bilicki et al., 2021). This is in contrast to other dynamical masses presented in the literature: such measurements are based on expensive spectroscopic data (see e.g. Rines et al., 2016) and are found to produce masses higher than lensing estimates (Herbonnet et al., 2020), an effect which might be due to systematic selection biases afflicting these more precise measurements (Old et al., 2015).

Because the relation between r_{sp} and halo mass depends on cosmology, this measurement naturally provides a constraint on structure formation, although the precision is relatively low with current data. The predictions for splashback also have trends with redshift, mass, and galaxy properties that are expected to be informative (Xhakaj et al., 2020; Shin et al., 2021). By comparing splashback and lensing masses, we were able to constrain the effects on r_{sp} of deviations from GR in a relatively straightforward manner. In this case, the interpretation of the difference between dynamical mass and lensing mass is not a simple rescaling, but it is connected to the full trajectory of the infalling material. By performing this measurement as a function of redshift, it is in principle possible to track the effects as a function of cosmic time and disentangle the effects of the accretion rate from the effect of fifth forces.

Precise measurements of the outer edge of massive dark matter halos have become feasible only in the last decade, thanks to the introduction of large galaxy and cluster samples. These measurements allow the study of the interface between the nonlinear multi-stream region of collapsed structures and the mildly nonlinear scales of infalling material, and directly connect the environment of massive halos and their properties. As we have shown in this work, this new research direction offers a route to reliable dynamical mass measurements as well as a new way to probe gravitational theories.

As discussed in Section 5.5.2, future stage IV surveys will provide percentage level splashback measurements. Modeling the trends in redshift, mass, accretion rate, and satellite properties of this feature promises to provide a powerful probe of the physics behind galaxy formation (Adhikari et al., 2020), as well as the large-scale environment of massive halos and their anisotropy (Contigiani et al., 2021).

Bibliography

Susmita Adhikari, Neal Dalal, and Robert T. Chamberlain. Splashback in accreting dark matter halos. *Journal of Cosmology and Astroparticle Physics*, 2014(11):019–019, November 2014. ISSN 1475-7516. doi: 10.1088/1475-7516/2014/11/019.

Susmita Adhikari, Neal Dalal, and Joseph Clampitt. Observing dynamical friction in galaxy clusters. *J. Cosmology Astropart. Phys.*, 2016(7):022, July 2016. doi: 10.1088/1475-7516/2016/07/022.

Susmita Adhikari, Tae-hyeon Shin, Bhuvnesh Jain, Matt Hilton, Eric Baxter, Chihway Chang, Risa H. Wechsler, Nick Battaglia, J. Richard Bond, Sebastian Bocquet, Joseph DeRose, Steve K. Choi, Mark Devlin, Jo Dunkley, August E. Evrard, Simone Ferraro, J. Colin Hill, John P. Hughes, Patricio A. Gallardo, Martine Lokken, Amanda MacInnis, Jeffrey McMahon, Mathew S. Madhavacheril, Federico Nati, Laura B. Newburgh, Michael D. Niemack, Lyman A. Page, Antonella Palmese, Bruce Partridge, Eduardo Rozo, Eli Rykoff, Maria Salatino, Alessandro Schillaci, Neelima Sehgal, Cristóbal Sifón, Chun-Hao To, Ed Wollack, Hao-Yi Wu, Zhilei Xu, Michel Aguena, Sahar Alam, Alexandra Amon, James Annis, Santiago Avila, David Bacon, Emmanuel Bertin, Sunayana Bhargava, David Brooks, David L. Burke, Aurelio C. Rosell, Matias Carrasco Kind, Jorge Carretero, Francisco Javier Castander, Ami Choi, Matteo Costanzi, Luiz N. da Costa, Juan De Vicente, Shantanu Desai, Thomas H. Diehl, Peter Doel, Spencer Everett, Ismael Ferrero, Agnès Ferté, Brenna Flaugher, Pablo Fosalba, Josh Frieman, Juan García-Bellido, Enrique Gaztanaga, Daniel Gruen, Robert A. Gruendl, Julia Gschwend, Gaston Gutierrez, Will G. Hartley, Samuel R. Hinton, Devon L. Hollowood, Klaus Honscheid, David J. James, Tesla Jeltema, Kyler Kuehn, Nikolay Kuropatkin, Ofer Lahav, Marcos Lima, Marcio A. G. Maia, Jennifer L. Marshall, Paul Martini, Peter Melchior, Felipe Menanteau, Ramon Miquel, Robert Morgan, Ricardo L. C. Ogando, Francisco Paz-Chinchón, Andrés Plazas Malagón, Eusebio Sanchez, Basilio Santiago, Vic Scarpine, Santiago Serrano, Ignacio Sevilla-Noarbe, Mathew Smith, Marcelle Soares-Santos, Eric Suchyta, Molly E. C. Swanson, Tamas N. Varga, Reese D. Wilkinson, Yuanyuan Zhang, Jason E. Austermann, James A. Beall, Daniel T. Becker, Edward V. Denison, Shannon M. Duff, Gene C. Hilton, Johannes Hubmayr,

- Joel N. Ullom, Jeff Van Lanen, Leila R. Vale, DES Collaboration, and ACT Collaboration. Probing galaxy evolution in massive clusters using ACT and DES: splashback as a cosmic clock. *arXiv e-prints*, art. arXiv:2008.11663, August 2020.
- Andreas Albrecht, Gary Bernstein, Robert Cahn, Wendy L. Freedman, Jacqueline Hewitt, Wayne Hu, John Huth, Marc Kamionkowski, Edward W. Kolb, Lloyd Knox, John C. Mather, Suzanne Staggs, and Nicholas B. Suntzeff. Report of the Dark Energy Task Force. *arXiv e-prints*, art. astro-ph/0609591, September 2006.
- Luca Amendola, Martin Kunz, and Domenico Sapone. Measuring the dark side (with weak lensing). *J. Cosmology Astropart. Phys.*, 2008(4):013, April 2008. doi: 10.1088/1475-7516/2008/04/013.
- S. Arnouts and O. Ilbert. LePHARE: Photometric Analysis for Redshift Estimate, August 2011.
- Arka Banerjee, Susmita Adhikari, Neal Dalal, Surhud More, and Andrey Kravtsov. Signatures of self-interacting dark matter on cluster density profile and subhalo distributions. *J. Cosmology Astropart. Phys.*, 2020(2):024, February 2020. doi: 10.1088/1475-7516/2020/02/024.
- James M. Bardeen. Gauge-invariant cosmological perturbations. *Phys. Rev. D*, 22(8):1882–1905, October 1980. doi: 10.1103/PhysRevD.22.1882.
- Eric Baxter, Chihway Chang, Bhuvnesh Jain, Susmita Adhikari, Neal Dalal, Andrey Kravtsov, Surhud More, Eduardo Rozo, Eli Rykoff, and Ravi K. Sheth. The Halo Boundary of Galaxy Clusters in the SDSS. *ApJ*, 841(1):18, May 2017. doi: 10.3847/1538-4357/aa6ff0.
- B. Bertotti, L. Iess, and P. Tortora. A test of general relativity using radio links with the Cassini spacecraft. *Nature*, 425(6956):374–376, September 2003. doi: 10.1038/nature01997.
- Edmund Bertschinger and Phillip Zukin. Distinguishing modified gravity from dark energy. *Phys. Rev. D*, 78(2):024015, July 2008. doi: 10.1103/PhysRevD.78.024015.
- Suman Bhattacharya, Salman Habib, Katrin Heitmann, and Alexey Vikhlinin. Dark Matter Halo Profiles of Massive Clusters: Theory versus Observations. *ApJ*, 766(1):32, March 2013. doi: 10.1088/0004-637X/766/1/32.
- M. Bilicki, A. Dvornik, H. Hoekstra, A. H. Wright, N. E. Chisari, M. Vakili, M. Asgari, B. Giblin, C. Heymans, H. Hildebrandt, B. W. Holwerda, A. Hopkins, H. Johnston, A. Kannawadi, K. Kuijken, S. J. Nakoneczny, H. Y. Shan, A. Sonnenfeld, and E. Valentijn. Bright galaxy sample in the Kilo-Degree Survey Data Release 4: selection, photometric redshifts, and physical properties. *arXiv e-prints*, art. arXiv:2101.06010, January 2021.

- Adam S. Bolton, Saul Rappaport, and Scott Burles. Constraint on the Post-Newtonian Parameter γ on Galactic Size Scales. *Phys. Rev. D*, 74:061501, 2006. doi: 10.1103/PhysRevD.74.061501.
- Clare Burrage and Jeremy Sakstein. Tests of chameleon gravity. *Living Reviews in Relativity*, 21(1):1, March 2018. doi: 10.1007/s41114-018-0011-x.
- Philipp Busch and Simon D. M. White. Assembly bias and splashback in galaxy clusters. *Monthly Notices of the Royal Astronomical Society*, 470(4):4767–4781, June 2017. ISSN 1365-2966. doi: 10.1093/mnras/stx1584.
- DES Collaboration. The Splashback Feature around DES Galaxy Clusters: Galaxy Density and Weak Lensing Profiles. *ApJ*, 864(1):83, September 2018. doi: 10.3847/1538-4357/aad5e7.
- Planck Collaboration. Planck 2015 results. *Astronomy & Astrophysics*, 594:A1, September 2016. ISSN 1432-0746. doi: 10.1051/0004-6361/201527101.
- Thomas E. Collett, Lindsay J. Oldham, Russell J. Smith, Matthew W. Auger, Kyle B. Westfall, David Bacon, Robert C. Nichol, Karen L. Masters, Kazuya Koyama, and Remco van den Bosch. A precise extragalactic test of General Relativity. *Science*, 360(6395):1342–1346, June 2018. doi: 10.1126/science.aao2469.
- O. Contigiani, Y. M. Bahé, and H. Hoekstra. The mass-size relation of galaxy clusters. *MNRAS*, May 2021. doi: 10.1093/mnras/stab1463.
- Omar Contigiani, Henk Hoekstra, and Yannick M. Bahé. Weak lensing constraints on splashback around massive clusters. *MNRAS*, 485(1):408–415, May 2019. doi: 10.1093/mnras/stz404.
- Omar Contigiani, Valeri Vardanyan, and Alessandra Silvestri. Splashback radius in symmetron gravity. *Physical Review D*, 99(6), March 2019. ISSN 2470-0029. doi: 10.1103/physrevd.99.064030.
- J. T. A. de Jong, G. A. Verdoes Kleijn, K. H. Kuijken, and E. A. Valentijn. The Kilo-Degree Survey. *Experimental Astronomy*, 35:25–44, January 2013. doi: 10.1007/s10686-012-9306-1.
- Benedikt Diemer. The splashback radius of halos from particle dynamics. i. the sparta algorithm. *The Astrophysical Journal Supplement Series*, 231(1):5, July 2017. ISSN 1538-4365. doi: 10.3847/1538-4365/aa799c.
- Benedikt Diemer. COLOSSUS: A python toolkit for cosmology, large-scale structure, and dark matter halos. *Astrophys. J. Suppl.*, 239(2):35, 2018. doi: 10.3847/1538-4365/aee8c.

- Benedikt Diemer. Universal at Last? The Splashback Mass Function of Dark Matter Halos. *ApJ*, 903(2):87, November 2020a. doi: 10.3847/1538-4357/abbf52.
- Benedikt Diemer. The Splashback Radius of Halos from Particle Dynamics. III. Halo Catalogs, Merger Trees, and Host-Subhalo Relations. *ApJS*, 251(2):17, December 2020b. doi: 10.3847/1538-4365/abbf51.
- Benedikt Diemer and Andrey V. Kravtsov. Dependence of the Outer Density Profiles of Halos on Their Mass Accretion Rate. *ApJ*, 789(1):1, July 2014. doi: 10.1088/0004-637X/789/1/1.
- Benedikt Diemer and Andrey V. Kravtsov. A Universal Model for Halo Concentrations. *ApJ*, 799(1):108, January 2015. doi: 10.1088/0004-637X/799/1/108.
- Benedikt Diemer, Surhud More, and Andrey V. Kravtsov. The Pseudo-evolution of Halo Mass. *ApJ*, 766(1):25, March 2013. doi: 10.1088/0004-637X/766/1/25.
- Benedikt Diemer, Philip Mansfield, Andrey V. Kravtsov, and Surhud More. The splashback radius of halos from particle dynamics. ii. dependence on mass, accretion rate, redshift, and cosmology. *The Astrophysical Journal*, 843(2):140, July 2017. ISSN 1538-4357. doi: 10.3847/1538-4357/aa79ab.
- Andrej Dvornik, Marcello Cacciato, Konrad Kuijken, Massimo Viola, Henk Hoekstra, Reiko Nakajima, Edo van Uitert, Margot Brouwer, Ami Choi, Thomas Erben, and et al. A kids weak lensing analysis of assembly bias in gama galaxy groups. *Monthly Notices of the Royal Astronomical Society*, 468(3):3251–3265, March 2017. ISSN 1365-2966. doi: 10.1093/mnras/stx705.
- A. Edge, W. Sutherland, K. Kuijken, S. Driver, R. McMahon, S. Eales, and J. P. Emerson. The VISTA Kilo-degree Infrared Galaxy (VIKING) Survey: Bridging the Gap between Low and High Redshift. *The Messenger*, 154:32–34, December 2013.
- J Einasto. On the Construction of a Composite Model for the Galaxy and on the Determination of the System of Galactic Parameters. *Trudy Astrofizicheskogo Instituta Alma-Ata*, 5:87–100, 1965.
- T. Erben, M. Schirmer, J. P. Dietrich, O. Cordes, L. Haberzettl, M. Hettterscheidt, H. Hildebrandt, O. Schmithuesen, P. Schneider, P. Simon, E. Deul, R. N. Hook, N. Kaiser, M. Radovich, C. Benoist, M. Nonino, L. F. Olsen, I. Prandoni, R. Wichmann, S. Zaggia, D. Bomans, R. J. Dettmar, and J. M. Miralles. GaBoDS: The Garching-Bonn Deep Survey. IV. Methods for the image reduction of multi-chip cameras demonstrated on data from the ESO Wide-Field Imager. *Astronomische Nachrichten*, 326(6):432–464, July 2005. doi: 10.1002/asna.200510396.

- I. Fenech Conti, Ricardo Herbonnet, Henk Hoekstra, Julian Merten, Lance Miller, and Massimo Viola. Calibration of weak-lensing shear in the Kilo-Degree Survey. *Mon. Not. Roy. Astron. Soc.*, 467(2):1627–1651, 2017. doi: 10.1093/mnras/stx200.
- Daniel Foreman-Mackey, David W. Hogg, Dustin Lang, and Jonathan Goodman. emcee: The MCMC Hammer. *Publications of the Astronomical Society of the Pacific*, 125(925): 306–312, March 2013. ISSN 00046280. doi: 10.1086/670067.
- Maria Cristina Fortuna, Henk Hoekstra, Harry Johnston, Mohammadjavad Vakili, Arun Kannawadi, Christos Georgiou, Benjamin Joachimi, Angus H. Wright, Marika Asgari, Maciej Bilicki, Catherine Heymans, Hendrik Hildebrandt, Konrad Kuijken, and Maximilian von Wietersheim-Kramsta. 2021.
- Liang Gao, Julio F. Navarro, Shaun Cole, Carlos S. Frenk, Simon D. M. White, Volker Springel, Adrian Jenkins, and Angelo F. Neto. The redshift dependence of the structure of massive Λ cold dark matter haloes. *Monthly Notices of the Royal Astronomical Society*, 387(2):536–544, June 2008. ISSN 0035-8711. doi: 10.1111/j.1365-2966.2008.13277.x.
- Michael D. Gladders and H. K. C. Yee. A New Method For Galaxy Cluster Detection. I. The Algorithm. *AJ*, 120(4):2148–2162, October 2000. doi: 10.1086/301557.
- Ricardo Herbonnet, Cristóbal Sifón, Henk Hoekstra, Yannick Bahé, Remco F. J. van der Burg, Jean-Baptiste Melin, Anja von der Linden, David Sand, Scott Kay, and David Barnes. CCCP and MENeCS: (updated) weak-lensing masses for 100 galaxy clusters. *MNRAS*, 497(4):4684–4703, October 2020. doi: 10.1093/mnras/staa2303.
- Kurt Hinterbichler, Justin Khoury, Aaron Levy, and Andrew Matas. Symmetron cosmology. *Phys. Rev. D*, 84(10):103521, November 2011. doi: 10.1103/PhysRevD.84.103521.
- M. Jarvis, G. Bernstein, and B. Jain. The skewness of the aperture mass statistic. *MNRAS*, 352(1):338–352, July 2004. doi: 10.1111/j.1365-2966.2004.07926.x.
- Mike Jarvis. TreeCorr: Two-point correlation functions, August 2015.
- Shahab Joudaki, Chris Blake, Andrew Johnson, Alexandra Amon, Marika Asgari, Ami Choi, Thomas Erben, Karl Glazebrook, Joachim Harnois-Déraps, Catherine Heymans, Hendrik Hildebrandt, Henk Hoekstra, Dominik Klaes, Konrad Kuijken, Chris Lidman, Alexander Mead, Lance Miller, David Parkinson, Gregory B. Poole, Peter Schneider, Massimo Viola, and Christian Wolf. KiDS-450 + 2dFLenS: Cosmological parameter constraints from weak gravitational lensing tomography and overlapping redshift-space galaxy clustering. *MNRAS*, 474(4):4894–4924, March 2018. doi: 10.1093/mnras/stx2820.

- Arun Kannawadi, Henk Hoekstra, Lance Miller, Massimo Viola, Ian Fenech Conti, Riccardo Herbonnet, Thomas Erben, Catherine Heymans, Hendrik Hildebrandt, Konrad Kuijken, Mohammadjavad Vakili, and Angus H. Wright. Towards emulating cosmic shear data: revisiting the calibration of the shear measurements for the Kilo-Degree Survey. *A&A*, 624:A92, April 2019. doi: 10.1051/0004-6361/201834819.
- K. Kuijken, C. Heymans, A. Dvornik, H. Hildebrandt, J. T. A. de Jong, A. H. Wright, T. Erben, M. Bilicki, B. Giblin, H. Y. Shan, F. Getman, A. Grado, H. Hoekstra, L. Miller, N. Napolitano, M. Paolilo, M. Radovich, P. Schneider, W. Sutherland, M. Tewes, C. Tortora, E. A. Valentijn, and G. A. Verdoes Kleijn. The fourth data release of the Kilo-Degree Survey: ugri imaging and nine-band optical-IR photometry over 1000 square degrees. *A&A*, 625:A2, May 2019. doi: 10.1051/0004-6361/201834918.
- R. B. Larson, B. M. Tinsley, and C. N. Caldwell. The evolution of disk galaxies and the origin of S0 galaxies. *ApJ*, 237:692–707, May 1980. doi: 10.1086/157917.
- R. Laureijs, J. Amiaux, S. Arduini, J. L. Auguères, J. Brinchmann, R. Cole, M. Cropper, C. Dabin, L. Duvet, A. Ealet, B. Garilli, P. Gondoin, L. Guzzo, J. Hoar, H. Hoekstra, R. Holmes, T. Kitching, T. Maciaszek, Y. Mellier, F. Pasian, W. Percival, J. Rhodes, G. Saavedra Criado, M. Sauvage, R. Scaramella, L. Valenziano, S. Warren, R. Bender, F. Castander, A. Cimatti, O. Le Fèvre, H. Kurki-Suonio, M. Levi, P. Lilje, G. Meylan, R. Nichol, K. Pedersen, V. Popa, R. Rebolo Lopez, H. W. Rix, H. Rottgering, W. Zeilinger, F. Grupp, P. Hudelot, R. Massey, M. Meneghetti, L. Miller, S. Paltani, S. Paulin-Henriksson, S. Pires, C. Saxton, T. Schrabback, G. Seidel, J. Walsh, N. Aghanim, L. Amendola, J. Bartlett, C. Baccigalupi, J. P. Beaulieu, K. Benabed, J. G. Cuby, D. Elbaz, P. Fosalba, G. Gavazzi, A. Helmi, I. Hook, M. Irwin, J. P. Kneib, M. Kunz, F. Mannucci, L. Moscardini, C. Tao, R. Teyssier, J. Weller, G. Zamorani, M. R. Zapatero Osorio, O. Boulade, J. J. Fomond, A. Di Giorgio, P. Guttridge, A. James, M. Kemp, J. Martignac, A. Spencer, D. Walton, T. Blümchen, C. Bonoli, F. Bortoletto, C. Cerna, L. Corcione, C. Fabron, K. Jahnke, S. Ligori, F. Madrid, L. Martin, G. Morgante, T. Pamplona, E. Prieto, M. Riva, R. Toledo, M. Trifoglio, F. Zerbi, F. Abdalla, M. Douspis, C. Grenet, S. Borgani, R. Bouwens, F. Courbin, J. M. Delouis, P. Dubath, A. Fontana, M. Frailis, A. Grazian, J. Koppenhöfer, O. Mansutti, M. Melchior, M. Mignoli, J. Mohr, C. Neissner, K. Noddle, M. Poncet, M. Scodeggio, S. Serrano, N. Shane, J. L. Starck, C. Surace, A. Taylor, G. Verdoes-Kleijn, C. Vuerli, O. R. Williams, A. Zacchei, B. Altieri, I. Escudero Sanz, R. Kohley, T. Oosterbroek, P. Astier, D. Bacon, S. Bardelli, C. Baugh, F. Bellagamba, C. Benoist, D. Bianchi, A. Biviano, E. Branchini, C. Carbone, V. Cardone, D. Clements, S. Colombi, C. Conselice, G. Cresci, N. Deacon, J. Dunlop, C. Fedeli, F. Fontanot, P. Franzetti, C. Giocoli, J. Garcia-Bellido, J. Gow, A. Heavens, P. Hewett, C. Heymans, A. Holland, Z. Huang, O. Ilbert, B. Joachimi, E. Jennins, E. Kerins, A. Kiessling, D. Kirk, R. Kotak, O. Krause, O. Lahav, F. van Leeuwen, J. Lesgourgues, M. Lombardi, M. Magliocchetti, K. Maguire, E. Majerotto, R. Maoli, F. Marulli, S. Maurogordato, H. McCracken,

- R. McLure, A. Melchiorri, A. Merson, M. Moresco, M. Nonino, P. Norberg, J. Peacock, R. Pello, M. Penny, V. Pettorino, C. Di Porto, L. Pozzetti, C. Quercellini, M. Radovich, A. Rassat, N. Roche, S. Ronayette, E. Rossetti, B. Sartoris, P. Schneider, E. Semboloni, S. Serjeant, F. Simpson, C. Skordis, G. Smadja, S. Smartt, P. Spano, S. Spiro, M. Sullivan, A. Tilquin, R. Trotta, L. Verde, Y. Wang, G. Williger, G. Zhao, J. Zoubian, and E. Zucca. Euclid definition study report, 2011.
- D. Nelson Limber. The Analysis of Counts of the Extragalactic Nebulae in Terms of a Fluctuating Density Field. *ApJ*, 117:134, January 1953. doi: 10.1086/145672.
- LSST Science Collaboration, Paul A. Abell, Julius Allison, Scott F. Anderson, John R. Andrew, J. Roger P. Angel, Lee Armus, David Arnett, S. J. Asztalos, Tim S. Axelrod, and et al. LSST Science Book, Version 2.0. *arXiv e-prints*, art. arXiv:0912.0201, December 2009.
- Conor L. Mancone and Anthony H. Gonzalez. EzGal: A Flexible Interface for Stellar Population Synthesis Models. *PASP*, 124(916):606, June 2012. doi: 10.1086/666502.
- Rachel Mandelbaum, Uroš Seljak, Guinevere Kauffmann, Christopher M. Hirata, and Jonathan Brinkmann. Galaxy halo masses and satellite fractions from galaxy-galaxy lensing in the Sloan Digital Sky Survey: stellar mass, luminosity, morphology and environment dependencies. *MNRAS*, 368(2):715–731, May 2006. doi: 10.1111/j.1365-2966.2006.10156.x.
- John P. McFarland, Gijs Verdoes-Kleijn, Gert Sikkema, Ewout M. Helmich, Danny R. Boxhoorn, and Edwin A. Valentijn. The Astro-WISE optical image pipeline. Development and implementation. *Experimental Astronomy*, 35(1-2):45–78, January 2013. doi: 10.1007/s10686-011-9266-x.
- L. Miller, C. Heymans, T. D. Kitching, L. van Waerbeke, T. Erben, H. Hildebrandt, H. Hoekstra, Y. Mellier, B. T. P. Rowe, J. Coupon, J. P. Dietrich, L. Fu, J. Harnois-Déraps, M. J. Hudson, M. Kilbinger, K. Kuijken, T. Schrabback, E. Semboloni, S. Vafaei, and M. Velander. Bayesian galaxy shape measurement for weak lensing surveys - III. Application to the Canada-France-Hawaii Telescope Lensing Survey. *MNRAS*, 429(4):2858–2880, March 2013. doi: 10.1093/mnras/sts454.
- Ben Moore, Neal Katz, George Lake, Alan Dressler, and Augustus Oemler. Galaxy harassment and the evolution of clusters of galaxies. *Nature*, 379(6566):613–616, February 1996. doi: 10.1038/379613a0.
- Surhud More, Benedikt Diemer, and Andrey V. Kravtsov. The splashback radius as a physical halo boundary and the growth of halo mass. *The Astrophysical Journal*, 810(1):36, August 2015. ISSN 1538-4357. doi: 10.1088/0004-637x/810/1/36.

- Surhud More, Hironao Miyatake, Masahiro Takada, Benedikt Diemer, Andrey V. Kravtsov, Neal K. Dalal, Anupreeta More, Ryoma Murata, Rachel Mandelbaum, Eduardo Rozo, Eli S. Rykoff, Masamune Oguri, and David N. Spergel. Detection of the Splashback Radius and Halo Assembly Bias of Massive Galaxy Clusters. *ApJ*, 825(1): 39, July 2016. doi: 10.3847/0004-637X/825/1/39.
- Julio F. Navarro, Carlos S. Frenk, and Simon D. M. White. The Structure of Cold Dark Matter Halos. *The Astrophysical Journal*, 462:563, May 1996. ISSN 0004-637X. doi: 10.1086/177173.
- Julio F. Navarro, Carlos S. Frenk, and Simon D. M. White. A Universal Density Profile from Hierarchical Clustering. *The Astrophysical Journal*, 490(2):493–508, December 1997. ISSN 0004-637X. doi: 10.1086/304888.
- Ciaran A. J. O’Hare and Clare Burrage. Stellar kinematics from the symmetron fifth force in the Milky Way disk. *Phys. Rev. D*, 98(6):064019, September 2018. doi: 10.1103/PhysRevD.98.064019.
- L. Old, R. Wojtak, G. A. Mamon, R. A. Skibba, F. R. Pearce, D. Croton, S. Bamford, P. Behroozi, R. de Carvalho, J. C. Muñoz-Cuartas, D. Gifford, M. E. Gray, A. von der Linden, M. R. Merrifield, S. I. Muldrew, V. Müller, R. J. Pearson, T. J. Ponman, E. Rozo, E. Rykoff, A. Saro, T. Sepp, C. Sifón, and E. Tempel. Galaxy Cluster Mass Reconstruction Project - II. Quantifying scatter and bias using contrasting mock catalogues. *MNRAS*, 449(2):1897–1920, May 2015. doi: 10.1093/mnras/stv421.
- Stephanie O’Neil, David J. Barnes, Mark Vogelsberger, and Benedikt Diemer. The splashback boundary of haloes in hydrodynamic simulations. *MNRAS*, 504(3):4649–4666, July 2021. doi: 10.1093/mnras/stab1221.
- L. Pizzuti, B. Sartoris, S. Borgani, L. Amendola, K. Umetsu, A. Biviano, M. Girardi, P. Rosati, I. Balestra, G. B. Caminha, B. Frye, A. Koekemoer, C. Grillo, M. Lombardi, A. Mercurio, and M. Nonino. CLASH-VLT: testing the nature of gravity with galaxy cluster mass profiles. *J. Cosmology Astropart. Phys.*, 2016(4):023, April 2016. doi: 10.1088/1475-7516/2016/04/023.
- Levon Pogosian, Alessandra Silvestri, Kazuya Koyama, and Gong-Bo Zhao. How to optimally parametrize deviations from general relativity in the evolution of cosmological perturbations. *Phys. Rev. D*, 81(10):104023, May 2010. doi: 10.1103/PhysRevD.81.104023.
- William H. Press and Paul Schechter. Formation of Galaxies and Clusters of Galaxies by Self-Similar Gravitational Condensation. *ApJ*, 187:425–438, February 1974. doi: 10.1086/152650.

- A. M. Price-Whelan et al. The Astropy Project: Building an Open-science Project and Status of the v2.0 Core Package. *Astron. J.*, 156(3):123, 2018. doi: 10.3847/1538-3881/aabc4f.
- Kenneth J. Rines, Margaret J. Geller, Antonaldo Diaferio, and Ho Seong Hwang. HeCS-SZ: The Hectospec Survey of Sunyaev-Zeldovich-selected Clusters. *ApJ*, 819(1):63, March 2016. doi: 10.3847/0004-637X/819/1/63.
- E. Rozo, E. S. Rykoff, A. Abate, C. Bonnett, M. Crocce, C. Davis, B. Hoyle, B. Leistedt, H. V. Peiris, R. H. Wechsler, T. Abbott, F. B. Abdalla, M. Banerji, A. H. Bauer, A. Benoit-Lévy, G. M. Bernstein, E. Bertin, D. Brooks, E. Buckley-Geer, D. L. Burke, D. Capozzi, A. Carnero Rosell, D. Carollo, M. Carrasco Kind, J. Carretero, F. J. Castander, M. J. Childress, C. E. Cunha, C. B. D’Andrea, T. Davis, D. L. DePoy, S. Desai, H. T. Diehl, J. P. Dietrich, P. Doel, T. F. Eifler, A. E. Evrard, A. Fausti Neto, B. Flaugher, P. Fosalba, J. Frieman, E. Gaztanaga, D. W. Gerdes, K. Glazebrook, D. Gruen, R. A. Gruendl, K. Honscheid, D. J. James, M. Jarvis, A. G. Kim, K. Kuehn, N. Kuropatkin, O. Lahav, C. Lidman, M. Lima, M. A. G. Maia, M. March, P. Martini, P. Melchior, C. J. Miller, R. Miquel, J. J. Mohr, R. C. Nichol, B. Nord, C. R. O’Neill, R. Ogando, A. A. Plazas, A. K. Romer, A. Roodman, M. Sako, E. Sanchez, B. Santiago, M. Schubnell, I. Sevilla-Noarbe, R. C. Smith, M. Soares-Santos, F. Sobreira, E. Suchyta, M. E. C. Swanson, J. Thaler, D. Thomas, S. Uddin, V. Vikram, A. R. Walker, W. Wester, Y. Zhang, and L. N. da Costa. redMaGiC: selecting luminous red galaxies from the DES Science Verification data. *MNRAS*, 461(2):1431–1450, September 2016. doi: 10.1093/mnras/stw1281.
- Joop Schaye, Claudio Dalla Vecchia, C. M. Booth, Robert P. C. Wiersma, Tom Theuns, Marcel R. Haas, Serena Bertone, Alan R. Duffy, I. G. McCarthy, and Freeke van de Voort. The physics driving the cosmic star formation history. *MNRAS*, 402(3):1536–1560, March 2010. doi: 10.1111/j.1365-2966.2009.16029.x.
- Mauro Sereno, Cosimo Fedeli, and Lauro Moscardini. Comparison of weak lensing by NFW and Einasto halos and systematic errors. *J. Cosmology Astropart. Phys.*, 2016 (1):042, January 2016. doi: 10.1088/1475-7516/2016/01/042.
- Ravi K. Sheth and Giuseppe Tormen. On the environmental dependence of halo formation. *MNRAS*, 350(4):1385–1390, June 2004. doi: 10.1111/j.1365-2966.2004.07733.x.
- T Shin, S Adhikari, E J Baxter, C Chang, B Jain, N Battaglia, L Bleem, S Bocquet, J DeRose, D Gruen, and et al. Measurement of the splashback feature around sz-selected galaxy clusters with des, spt, and act. *Monthly Notices of the Royal Astronomical Society*, 487(2):2900–2918, May 2019. ISSN 1365-2966. doi: 10.1093/mnras/stz1434.
- T. Shin, B. Jain, S. Adhikari, E. J. Baxter, C. Chang, S. Pandey, A. Salcedo, D. H. Weinberg, A. Amsellem, N. Battaglia, M. Belyakov, T. Dacunha, S. Goldstein, A. V.

- Kravtsov, T. N. Varga, T. M. C. Abbott, M. Aguena, A. Alarcon, S. Allam, A. Amon, F. Andrade-Oliveira, J. Annis, D. Bacon, K. Bechtol, M. R. Becker, G. M. Bernstein, E. Bertin, S. Bocquet, J. R. Bond, D. Brooks, E. Buckley-Geer, D. L. Burke, A. Campos, A. Carnero Rosell, M. Carrasco Kind, J. Carretero, R. Chen, A. Choi, M. Costanzi, L. N. da Costa, J. DeRose, S. Desai, J. De Vicente, M. J. Devlin, H. T. Diehl, J. P. Dietrich, S. Dodelson, P. Doel, C. Doux, A. Drlica-Wagner, K. Eckert, J. Elvin-Poole, S. Everett, S. Ferraro, I. Ferrero, A. Ferté, B. Flaugher, J. Frieman, P. A. Gallardo, M. Gatti, E. Gaztanaga, D. W. Gerdes, D. Gruen, R. A. Gruendl, G. Gutierrez, I. Harrison, W. G. Hartley, J. C. Hill, M. Hilton, S. R. Hinton, D. L. Hollowood, J. P. Hughes, D. J. James, M. Jarvis, T. Jeltima, B. J. Koopman, E. Krause, K. Kuehn, N. Kuropatkin, O. Lahav, M. Lima, M. Lokken, N. MacCrann, M. S. Madhavacheril, M. A. G. Maia, J. McCullough, J. McMahon, P. Melchior, F. Menanteau, R. Miquel, J. J. Mohr, K. Moodley, R. Morgan, J. Myles, F. Nati, A. Navarro-Alsina, M. D. Niemack, R. L. C. Ogando, L. A. Page, A. Palmese, B. Partridge, F. Paz-Chinchón, M. E. S. Pereira, A. Pieres, A. A. Plazas Malagón, J. Prat, M. Raveri, M. Rodriguez-Monroy, R. P. Rollins, A. K. Romer, E. S. Rykoff, M. Salatino, C. Sánchez, E. Sanchez, B. Santiago, V. Scarpine, A. Schillaci, L. F. Secco, S. Serrano, I. Sevilla-Noarbe, E. Sheldon, B. D. Sherwin, C. Sifón, M. Smith, M. Soares-Santos, S. T. Staggs, E. Suchyta, M. E. C. Swanson, G. Tarle, D. Thomas, C. To, M. A. Troxel, I. Tutusaus, E. M. Vavagiakis, J. Weller, E. J. Wollack, B. Yanny, B. Yin, and Y. Zhang. The mass and galaxy distribution around SZ-selected clusters. *Monthly Notices of the Royal Astronomical Society*, (4):5758–5779, September 2021.
- Fergus Simpson, Catherine Heymans, David Parkinson, Chris Blake, Martin Kilbinger, Jonathan Benjamin, Thomas Erben, Hendrik Hildebrandt, Henk Hoekstra, Thomas D. Kitching, Yannick Mellier, Lance Miller, Ludovic Van Waerbeke, Jean Coupon, Liping Fu, Joachim Harnois-Déraps, Michael J. Hudson, Koenraad Kuijken, Barnaby Rowe, Tim Schrabback, Elisabetta Semboloni, Sanaz Vafaei, and Malin Velander. CFHTLenS: testing the laws of gravity with tomographic weak lensing and redshift-space distortions. *MNRAS*, 429(3):2249–2263, March 2013. doi: 10.1093/mnras/sts493.
- Rachel S. Somerville, Philip F. Hopkins, Thomas J. Cox, Brant E. Robertson, and Lars Hernquist. A semi-analytic model for the co-evolution of galaxies, black holes and active galactic nuclei. *MNRAS*, 391(2):481–506, December 2008. doi: 10.1111/j.1365-2966.2008.13805.x.
- Iskra Strateva, Željko Ivezić, Gillian R. Knapp, Vijay K. Narayanan, Michael A. Strauss, James E. Gunn, Robert H. Lupton, David Schlegel, Neta A. Bahcall, Jon Brinkmann, Robert J. Brunner, Tamás Budavári, István Csabai, Francisco Javier Castander, Mamoru Doi, Masataka Fukugita, Zsuzsanna Györy, Masaru Hamabe, Greg Hennessy, Takashi Ichikawa, Peter Z. Kunszt, Don Q. Lamb, Timothy A. McKay, Sadanori Okamura, Judith Racusin, Maki Sekiguchi, Donald P. Schneider, Kazuhiro Shimasaku, and Donald York. Color Separation of Galaxy Types in the Sloan Digital Sky Survey Imaging Data. *AJ*, 122(4):1861–1874, October 2001. doi: 10.1086/323301.

- Jeremy Tinker, Andrey V. Kravtsov, Anatoly Klypin, Kevork Abazajian, Michael Warren, Gustavo Yepes, Stefan Gottlöber, and Daniel E. Holz. Toward a Halo Mass Function for Precision Cosmology: The Limits of Universality. *ApJ*, 688(2):709–728, December 2008. doi: 10.1086/591439.
- Jeremy L. Tinker, Brant E. Robertson, Andrey V. Kravtsov, Anatoly Klypin, Michael S. Warren, Gustavo Yepes, and Stefan Gottlöber. The Large-scale Bias of Dark Matter Halos: Numerical Calibration and Model Tests. *ApJ*, 724(2):878–886, December 2010. doi: 10.1088/0004-637X/724/2/878.
- James W. Trayford, Tom Theuns, Richard G. Bower, Joop Schaye, Michelle Furlong, Matthieu Schaller, Carlos S. Frenk, Robert A. Crain, Claudio Dalla Vecchia, and Ian G. McCarthy. Colours and luminosities of $z = 0.1$ galaxies in the EAGLE simulation. *MNRAS*, 452(3):2879–2896, September 2015. doi: 10.1093/mnras/stv1461.
- Keiichi Umetsu and Benedikt Diemer. Lensing Constraints on the Mass Profile Shape and the Splashback Radius of Galaxy Clusters. *ApJ*, 836(2):231, February 2017. doi: 10.3847/1538-4357/aa5c90.
- Mohammadjavad Vakili, Maciej Bilicki, Henk Hoekstra, Nora Elisa Chisari, Michael J. I. Brown, Christos Georgiou, Arun Kannawadi, Konrad Kuijken, and Angus H. Wright. Luminous red galaxies in the Kilo-Degree Survey: selection with broad-band photometry and weak lensing measurements. *MNRAS*, 487(3):3715–3733, August 2019. doi: 10.1093/mnras/stz1249.
- Mohammadjavad Vakili, Henk Hoekstra, Maciej Bilicki, Maria-Cristina Fortuna, Konrad Kuijken, Angus H. Wright, Marika Asgari, Michael Brown, Elisabeth Dombrovskij, Thomas Erben, Benjamin Giblin, Catherine Heymans, Hendrik Hildebrandt, Harry Johnston, Shahab Joudaki, and Arun Kannawadi. Clustering of red-sequence galaxies in the fourth data release of the Kilo-Degree Survey. *arXiv e-prints*, art. arXiv:2008.13154, August 2020.
- Frank C. van den Bosch, Daniel Aquino, Xiaohu Yang, H. J. Mo, Anna Pasquali, Daniel H. McIntosh, Simone M. Weinmann, and Xi Kang. The importance of satellite quenching for the build-up of the red sequence of present-day galaxies. *MNRAS*, 387(1):79–91, June 2008. doi: 10.1111/j.1365-2966.2008.13230.x.
- Edo van Uitert, Marcello Cacciato, Henk Hoekstra, and Ricardo Herbonnet. Evolution of the luminosity-to-halo mass relation of LRGs from a combined analysis of SDSS-DR10+RCS2. *A&A*, 579:A26, July 2015. doi: 10.1051/0004-6361/201525834.
- M. Viola, M. Cacciato, M. Brouwer, K. Kuijken, H. Hoekstra, P. Norberg, A. S. G. Robotham, E. van Uitert, M. Alpaslan, I. K. Baldry, A. Choi, J. T. A. de Jong, S. P. Driver, T. Erben, A. Grado, Alister W. Graham, C. Heymans, H. Hildebrandt, A. M.

Hopkins, N. Irisarri, B. Joachimi, J. Loveday, L. Miller, R. Nakajima, P. Schneider, C. Sifón, and G. Verdoes Kleijn. Dark matter halo properties of GAMA galaxy groups from 100 square degrees of KiDS weak lensing data. *MNRAS*, 452(4):3529–3550, October 2015. doi: 10.1093/mnras/stv1447.

Harry Wilcox, David Bacon, Robert C. Nichol, Philip J. Rooney, Ayumu Terukina, A. Kathy Romer, Kazuya Koyama, Gong-Bo Zhao, Ross Hood, Robert G. Mann, Matt Hilton, Maria Manolopoulou, Martin Sahlén, Chris A. Collins, Andrew R. Liddle, Julian A. Mayers, Nicola Mehrtens, Christopher J. Miller, John P. Stott, and Pedro T. P. Viana. The XMM Cluster Survey: testing chameleon gravity using the profiles of clusters. *MNRAS*, 452(2):1171–1183, September 2015. doi: 10.1093/mnras/stv1366.

Enia Xhakaj, Benedikt Diemer, Alexie Leauthaud, Asher Wasserman, Song Huang, Yifei Luo, Susmita Adhikari, and Sukhdeep Singh. How accurately can we detect the splashback radius of dark matter haloes and its correlation with accretion rate? *MNRAS*, 499(3):3534–3543, December 2020. doi: 10.1093/mnras/staa3046.